Natural Resources for Human Health
eISSN: 2583-1194

Original Research

Received 25 March 2026
Revised 28 April 2026
Accepted 25 May 2026

Natural Resources for Human Health 2026, Vol. 6 (2s): 736–748

KEYWORDS:
Biosensors, Donnan potential, ion selective electrode, limit of detection, Poisson–Nernst–Planck model, potentiometry, sweat analysis, electrolyte monitoring.

A Unified Poisson-Nernst-Planck and Ion-Selective-Electrode Model for Sweat Electrolyte Analysis for Health Monitoring

Ms. Chaya H P[1], Dr. Shailaja K[2]

[1]Assistant professor, Department of Electronics and Instrumentation, SJCE, JSSSTU, Mysuru-570006,
Karnataka, India
chaya.hp@sjce.ac.in
[2]Professor, Department of Electronics and Instrumentation, SJCE, JSSSTU, Mysuru-570006
Karnataka, India
kshaila_15@sjce.ac.in
Corresponding Author: chaya.hp@sjce.ac.in

ABSTRACT: Potentiometric sweat sensors promise non-invasive, real-time monitoring of sodium (Na+), potassium (K+) and chloride (Cl−), yet their design is still dominated by trial-and-error prototyping because membrane-transport physics and analytical sensor calibration are typically modelled in separate, proprietary tools. This paper presents fully self-contained in-silico platform that unifies four physical layers of an ion-selective-electrode (ISE) sweat sensor within a single, dependency-free environment: (i) a one-dimensional Poisson–Nernst–Planck (PNP) model of multi-ion transport (Na+, K+, Cl−, H+, OH−) across a symmetric bipolar ion-selective membrane, including water dissociation and Donnan equilibria; (ii) a Nikolsky–Eisenman potentiometric response model with Debye–Huckel activity corrections; (iii) an analytical calibration and quantification module reporting slope (sensitivity), standard potential, coefficient of determination, limit of detection (LOD), linear range and recovery; and (iv) an electrode assembly voltage budget based on reversible water splitting thermodynamics and symmetric Butler–Volmer kinetics. The transport solver uses a Scharfetter–Gummel finite volume discretisation with an overflow safe Bernoulli flux, a Thomas tridiagonal solver and Gummel iteration, conserving total current to within 1–2%. The platform is parameterised with clinically measured mean sweat concentrations (Na+ 81.4, K+ 7.3, Cl− 88.1 mmol L−1) obtained on a Roche COBAS Pure 6 ISE analyser from 39 exercising participants. Simulated calibrations recover near Nernstian slopes (57–60 mV per decade), coefficients of determination R2 ≥ 0.9998 at a realistic 0.3 mV RMS noise level, LODs of the order of 10−2 mmol L−1 and analytical recoveries of 97.7–101%. The predicted limiting current density (≈20.5 A m−2) and Donnan driven concentration redistribution reproduce the expected electrodiffusive transport behaviour for this clinical composition. Because the entire tool executes offline as a single portable file, it lowers the barrier to reproducible, transparent sweat sensor design and can serve as a lightweight digital twin for pre-fabrication optimisation.

I. INTRODUCTION

Sweat is one of the few biofluids that human body makes available without a needle, kind of directly, almost. As an ultrafiltrate of blood plasma, it brings along electrolytes, metabolic residues, and hormones, and this is what makes it an option for non-invasive continuous physiological tracking [1], [2]. It may be obtained straight from the skin, and as it changes in relation to

hydration status, thermoregulatory stress and certain disease states, it has become one of the most sought-out targets of electrochemical biosensors – a rapidly developing type [3], [4], [5]. In practice, there are three major ions whose levels matter: sodium (Na^+), potassium (K^+), and chloride (Cl^-). Na^+ and Cl^- serve as proven markers of electrolyte imbalance, dehydration, and cystic fibrosis. Since K^+, being the main intracellular cation, remains stable throughout the process of ductal reabsorption, sweat analysis is often used as a proxy for intracellular status [6], [7], [8], [9]. The clinical significance goes beyond hydration. Hyponatremia, caused by decreased sodium concentrations, is an example of a dangerous, sometimes even life-threatening, fluid and electrolyte imbalance that occurs when exercising for long periods of time [10], while elevated sweat chloride concentration remains the gold standard for diagnosis of cystic fibrosis [11].So bringing these assessments out of the lab and into continuous, non-invasive monitoring depends on transducers where analytical performance sensitivity, detection limit, and accuracy over the relevant physiological concentration window are carefully benchmarked ahead of use. And that is exactly the design question this work addresses.

Potentiometric ion selective electrodes (ISEs) are the workhorse transducers for these ions in both benchtop analysers and miniaturised sensor platforms, owing to their near logarithmic response, low power requirement and straightforward multiplexing [12], [13], [14]. However, translating an ISE from a laboratory coupon to a reliable field deployable sensor requires simultaneous control of two coupled physical regimes that are seldom analysed together: (a) the electrodiffusive transport of ions across the ion selective membrane, which governs selectivity, response time and the limiting current, and (b) the thermodynamic and analytical response of the electrode, which governs sensitivity, detection limit and quantification accuracy. In current practice these regimes are typically studied with different, often proprietary, software packages finite element multiphysics suites for transport and separate statistical tools for calibration which hampers reproducibility and raises the barrier to entry for design stage optimisation [4], [15].

Despite this progress, membrane transport physics and the potentiometric measurement chain are almost always treated in isolation, with ion transport analysed in finite element multiphysics packages and electrode calibration handled by separate statistical workflows. As a result, a designer cannot readily trace how a change in membrane fixed charge, temperature or electrode slope propagates from ion transport through to the reported concentration and its analytical uncertainty. The present work removes this separation by evaluating both regimes within a single coupled model and grounding it in clinically measured sweat electrolyte concentrations (Na^+ 81.4, K^+ 7.3, Cl^- 88.1 mmol L^{-1}) acquired on a Roche COBAS Pure 6 ISE analyser from a cohort of 39 exercising participants.

This paper addresses that gap with a single, self-contained in-silico platform. Within one dependency-free environment it couples the four physical layers of an ISE sweat sensor that are usually modelled in isolation: PNP membrane transport, the potentiometric response, analytical calibration and quantification, and the electrode-assembly voltage budget. Its main contributions are three.

First, a coupled formulation:. One-dimensional multi-ion PNP transport - water dissociation and Donnan equilibria included – have been tied directly to a Nikolsky–Eisenman potentiometric response carrying Debye–Hückel activity corrections. Transport, thermodynamics and analytical performance are therefore evaluated on the same ion set and the same operating point, rather than stitched together from separate tools.

Second, an analytical quantification module: It takes simulated calibration data and turns it into the performance figures that really decide deployment: electrode slope (sensitivity) standard potential, coefficient of determination, residual standard deviation, limit of detection, linear range and analytical recovery, all of it while user-controlled measurement noise is present.

Lastly, a clinically derived benchmark: The platform is parameterised through measured sweat concentrations on a COBAS Pure 6 ISE analyser (Na^+ 81.4, K^+ 7.3, Cl^- 88.1 mmol L^{-1}), and it re-establishes the limiting-current density and physiological recoveries reported.

Then, the rest of the paper basically follows a simple flow. Section II provides literature review and motivation, and Section III constructs the unified computational framework. Section IV provides a self-contained implementation. Section V gives the result and discussion, including the benchmark against the clinical dataset. Limitations and scope are given in Section VI, while Section VII serves as the conclusion.

Natural Resources for Human Health
eISSN: 2583-1194

II. RELATED WORK AND MOTIVATION

While sweat sensing technology has come a long way since the early single-analyte demonstrators, today's systems are able to detect several electrolytes and metabolic markers simultaneously, almost in parallel [1], [3], [4], [16], [17]. Recent literature reviews highlight rapid progress in materials science, microfluidic sampling techniques and system integration; yet, again and again, the same persistent problems that hold it all back from clinical deployment re-surface – namely, the issues of stability, selectivity, and repeatability [4], [5], [15], [18]. Solid contact ISEs, in particular, have been validated for off-body sweat ion monitoring but remain sensitive to temperature, activity effects and drift, all of which are difficult to disentangle experimentally [14].

On the physiological side, controlled studies confirm that sweat Na+, K+ and Cl− vary strongly with sweat rate, fitness, acclimatisation, diet and time of day, so any sensor must operate accurately across a wide activity range [7], [19], [20], [21]. This variability underscores the need for design tools that quantify not only a nominal response but also the analytical uncertainty (LOD, recovery, linear range) across the physiological concentration window. Sampling and pre-analytical factors add further variance and are themselves an active research topic [22].

On the modelling side, PNP based descriptions of ion transport across ion exchange and bipolar membranes are well established and reproduce Donnan exclusion, concentration polarisation and limiting current behaviour. Such models are typically implemented in general purpose finite element multiphysics environments, which, although powerful, are proprietary, require substantial expertise and are not easily shared alongside a manuscript for independent verification. Conversely, the analytical performance of ISEs—slope, detection limit, recovery—is normally assessed with separate statistical workflows. To our knowledge, no lightweight, openly executable tool couples the two so that a designer can move seamlessly from membrane physics to reported concentration and its uncertainty. The platform described here is intended to fill that niche as a transparent, pre-fabrication digital twin.

III. UNIFIED COMPUTATIONAL FRAMEWORK

The framework comprises four coupled modules that share a common thermodynamic core (temperature, activity model and fundamental constants): (A) PNP membrane transport; (B) the numerical solver; (C) the potentiometric ISE response; (D) calibration and quantification; and (E) the electrode assembly voltage budget. Throughout, molar concentrations are expressed in mol m−3, which is numerically identical to mmol L−1, so all reported concentrations may be read directly in the clinical unit. Fundamental constants used are the Faraday constant F = 96 485.332 C mol−1, the molar gas constant R = 8.314 463 J mol−1 K−1, and a reference temperature T = 298.15 K (25 °C).

A. Poisson–Nernst–Planck Membrane Transport Model

In the present model, the computational domain is one-dimensional along *x* and consists of four subdomains: a stagnant diffusion layer (SDL), a cation selective membrane (CSM), an anion selective membrane (ASM) and a second SDL, forming a symmetric bipolar membrane (Fig. 2). The molar flux density Ni of species i is described by the Nernst–Planck equation, in which mobility has been eliminated through the Nernst–Einstein relation:

$$N_i = -\frac{D_i(dc_i)}{dx} - \frac{D_i}{RT} Z_i F \frac{c_i(d\varphi)}{dx} + vc_i \qquad (1)$$

where Di, ci and zi are the diffusion coefficient, molar concentration and charge number of species i, φ is the electric potential and v is the convective velocity, which is neglected in the SDLs for numerical stability. At steady state and in the absence of reaction the mass balance reduces to dNi/dx = Si, with the source term Si = 0 for the strong electrolyte ions Na+, K+ and Cl−. Hydrogen and hydroxide are coupled through the water self dissociation/recombination reaction

$$H_2O \rightleftharpoons H^+ + OH^-,\ S_{H^+} = S_{OH^-} = k_{b(K_w - c_{H^+}c_{OH^-})} \qquad (2)$$

where kb is the recombination rate constant and Kw the water autoprotolysis constant (Kw = 10−8 mol2 m−6 in the working units). The electric field is obtained from Poisson's equation, coupling the potential to the local space charge density and the membrane fixed charge:

$$\frac{d^2\varphi}{dx^2} = -\frac{F}{\varepsilon_0 \varepsilon_r}(\Sigma_i z_i c_i + z_{fix} c_{fix}) \qquad (3)$$

where ε0εr is the permittivity and zfixcfix is the fixed charge contribution of the membrane functional groups (cfix = 0 in the SDLs, negative in the CSM and positive in the ASM). The local current density follows from the charged species fluxes,

$$j = F \sum_i z_i N_i \quad (4)$$

and is spatially constant at steady state (dj/dx = 0) in the one-dimensional model, providing a strong internal consistency check. The specific conductivity follows as $\varkappa = (F2/RT) \sum i$ Di zi2 ci . From the same quantities the module also reports the ion-transport (transference) numbers ti = zi2Dici / ∑k zk2Dkck, which serve as diagnostic outputs and, by construction, sum to unity.

Drive the membrane hard enough in forward bias and the ion-exchange layers begin to run out of salt ions; the current then saturates at a limiting density. Setting the water-derived ions aside, the analytical limiting value used to cross-check the numerical solution is given by (5).

$$I_{lim} = -\frac{2F D_i}{X \delta_{mem}}(c_{Na^+} + c_{K^+} - c_{Cl^-})^2 \quad (5)$$

Where, X = membrane charge density, δ_{mem} = membrane thickness.

Boundary conditions fix electrolyte composition and pH at the outer SDL boundaries (perfectly stirred anolyte/catholyte), enforce electroneutrality and the H+/OH− equilibrium at both interfaces, set the potential reference at one boundary and the applied cell voltage U at the other, and impose continuity of concentrations, fluxes and current at internal interfaces where the Donnan condition generates the characteristic sharp concentration steps. The model input parameters are summarised in Table I.

Table I. Principal Input Parameters of the PNP Membrane Transport Model

Parameter	Symbol	Value
Ion-selective membrane thickness	L_{mem}	4×10^{-4} m
Stagnant diffusion layer thickness	L_{sdl}	1×10^{-4} m
Mean sweat Na^+ concentration	c_{Na}	81.4 mol m^{-3}
Mean sweat K^+ concentration	c_K	7.3 mol m^{-3}
Mean sweat Cl^- concentration	c_{Cl}	88.1 mol m^{-3}
Membrane fixed charge concentration	c_{fix}	1000 mol m^{-3}
Water autoprotolysis constant	K_w	1×10^{-8} mol^2 m^{-6}
Relative permittivity	ε_r	78
Temperature	T	298.15 K
Diffusivity of Na^+	D_{Na}	1.334×10^{-9} m^2 s^{-1}
Diffusivity of K^+	D_K	1.957×10^{-9} m^2 s^{-1}
Diffusivity of Cl^-	D_{Cl}	2.032×10^{-9} m^2 s^{-1}
Diffusivity of H^+	D_H	9.312×10^{-9} m^2 s^{-1}
Diffusivity of OH^-	D_{OH}	5.260×10^{-9} m^2 s^{-1}

The limiting cationic diffusivities of Na^+ and K^+ at 25 °C (1.334×10^{-9} and 1.957×10^{-9} m^2 s^{-1}) are adopted here for physical consistency with the aqueous transport literature; the remaining parameters are adopted from established values for ion exchange membrane systems.

Natural Resources for Human Health
eISSN: 2583-1194

B. Numerical Solution Strategy

Equations (1)–(4) constitute a stiff, nonlinearly coupled boundary value problem. They are discretised on a non-uniform mesh refined at the membrane–solution interfaces using a finite volume scheme. Interfacial fluxes are evaluated with the Scharfetter–Gummel exponential fitting formula, which remains stable in the migration dominated (high-Péclet) regime characteristic of the membrane interior. The exponential weighting uses an overflow safe implementation of the Bernoulli function $B(x) = x/(e^x - 1)$ with an appropriate small argument series expansion, preventing loss of precision when the local electric field is large. The resulting tridiagonal transport system is solved with the Thomas algorithm, and the coupled Nernst–Planck/Poisson system is advanced by Gummel (decoupled) iteration with under relaxation; the Poisson update is linearised in the Poisson–Boltzmann sense for stability. Two separate monitors observe the entire process of convergence. First of all, it is the residual of the fixed-point itself which is driven below a certain tolerance level, and then the iteration process just stops. The second monitor is more physical rather than numerical. As the steady-state current density j must remain constant over x, its dispersion over the mesh faces serves as a measure of accuracy which is not observed by the solver at all. Over the operating range we explored, that spread stays within 1–2 %, and the transference numbers add up to unity to within numerical tolerance.

C. Potentiometric Ion-Selective-Electrode Response Model

The transducer response is described by the Nikolsky–Eisenman equation, which generalises the Nernst relation to include the effect of interfering ions:

$$E = E^0 + s_i \log_{10}\left(a_i + \sum_{j \neq i} K_{ij}^{pot} a_j^{\frac{z_i}{z_j}}\right) \qquad (6)$$

Here E^0 is the standard (offset) potential, a_i the single-ion activity of the primary ion, K_{ij}^{pot} the potentiometric selectivity coefficient of interferent j, and s_i the electrode slope. We deliberately avoid the idealisation of a perfect Nernstian slope. Instead, every electrode carries a realistic, temperature-dependent slope,

$$s_i(T) = s_{i,0} \cdot \frac{T}{298.15} \qquad (7)$$

with $s_{i,0}$ the slope measured at 25 °C (Table II). Writing the slope this way keeps two things apart: the electrode's empirical, slightly sub-Nernstian behaviour, and the ideal thermodynamic value 2.303 RT/(z_iF)=59.16 mV per decade at 25 °C, which we retain only as a reference point.

$$\log_{10}\gamma_i = -\frac{A z_i^2 \sqrt{I}}{1 + \sqrt{I}}, \quad I = \frac{1}{2}\sum_k z_k^2 c_k \qquad (8)$$

with A = 0.509 $(\text{mol L}^{-1})^{-1/2}$ at 25 °C and I the ionic strength evaluated in molar concentration units (consistent with the tabulated coefficient A), so that $a_i = \gamma_i c_i$. The three primary electrodes (Na^+, K^+, Cl^-) plus the H^+ (glass) and OH^- references are parameterised as in Table II.

Table II. Default Electrode Parameters (25 °C)

Electrode	Slope $s_{i,0}$ (mV/decade)	Offset E0 (mV)	Sensing mechanism
Na^+	+58.0	+115	Glass / Na-ionophore membrane
K^+	+58.5	−80	Valinomycin membrane
Cl^-	−57.0	+45	Ag/AgCl (anionic response)
H^+	+58.8	+30	pH glass electrode
OH^-	−58.0	0	Reference/auxiliary

D. Calibration and Quantification

Calibration is performed for the three clinically reported ions (Na^+, K^+, Cl^-) using standard solutions spanning the physiological window: Na^+ {10, 40, 100}, K^+ {2, 6, 12} and Cl^- {10, 40, 100} mmol L^{-1}. For each standard, the electrode potential is generated from (6)–(8) and corrupted by additive Gaussian measurement noise of user selectable magnitude (default 0.3 mV

RMS), synthesised with the Box–Muller transform to emulate instrument and thermal noise. A weighted least squares fit of E versus $\log_{10}a_i$ yields the calibration slope s and intercept E^0, together with the coefficient of determination R^2 and the residual standard deviation

$$S_r = \sqrt{\frac{SS_{res}}{n-2}} \quad (9)$$

From these, the practical limit of detection and linear range are reported. The LOD is estimated from the calibration statistics as

$$LOD = c_{min} \cdot 10^{\frac{3S_r}{|s|}} \quad (10)$$

and unknown samples are back calculated by inverting (6) with the fitted parameters and the joint Debye–Huckel activity of the full sweat matrix, solved self consistently. Analytical accuracy is expressed as recovery,

$$\text{Recovery (\%)} = 100 \cdot \frac{c_{measured}}{c_{true}} \quad (11)$$

The module thus reports, per ion, the complete set of analytical figures of merit—sensitivity (slope), E^0, R^2, S_r, LOD, linear range and recovery—that determine fitness for practical use.

E. Electrode Assembly Voltage Budget

To relate the sensing membrane to a complete two electrode cell, an electrode assembly module computes the voltage budget for driving current through the assembly when water electrolysis is the faradaic process. The reversible cell voltage for water splitting is Erev = 1.23 V. The activation overpotential η at each electrode follows a symmetric Butler–Volmer relation,

$$j = 2\, j_0 \sinh\left(\frac{\alpha F\, \eta}{RT}\right) \quad (12)$$

with exchange current density j_0 and transfer coefficient α. The total applied voltage is the sum of the reversible term, the two activation overpotentials and the ohmic membrane drop U_m,

$$U = E_{rev} + 2\eta + U_m \quad (13)$$

and (12) (13) are solved for the operating point by bisection. To keep the assembly sweep fast, j(Um) is sampled on a small grid once and interpolated during the root finding, and a single shared table is reused across the temperature sweep.

IV. IMPLEMENTATION: A SELF CONTAINED IN-SILICO PLATFORM

All four modules are implemented in a single, self contained application that executes entirely in a standard web browser with no installation, server or network access. All that is needed for the tool is the numerical solver, interactive graphics, the 3D viewer, the symbolic math engine, and the report generation system, all of which work seamlessly out of the browser. The reviewer or collaborator simply opens the application locally and off-line and regenerates any graphic. This design directly addresses the reproducibility and accessibility concerns highlighted for sweat sensor research [4], [15]: the model, its parameters and its outputs travel together as a single artefact.

The interface exposes editable parameters for every module (membrane geometry and fixed charge, diffusivities, applied voltage, electrode slopes, offsets and selectivity coefficients, calibration standards, noise level and temperature), recomputes the affected outputs on demand, and can export a structured PDF report and comma separated calibration/quantification data. The overall architecture is shown in Fig. 1: clinically measured ISE concentrations parameterise the shared thermodynamic core, which feeds the transport, potentiometric, calibration and electrode assembly modules, whose outputs are combined into clinical interpretation bands and a reproducible report.

Natural Resources for Human Health
eISSN: 2583-1194

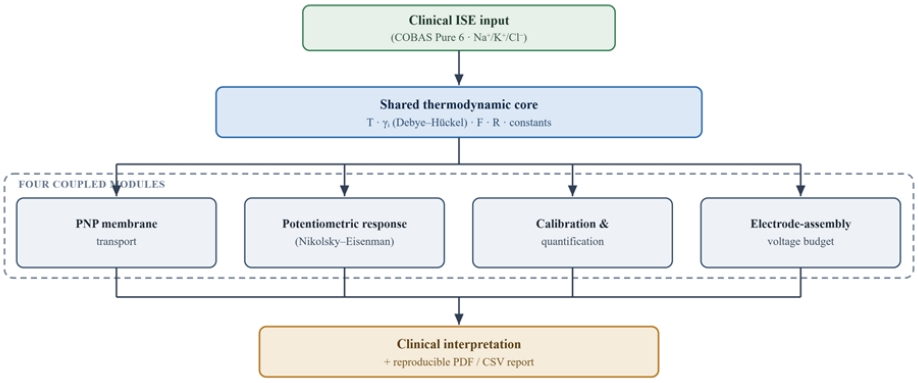

Fig. 1. Architecture of the unified in-silico platform. Clinically measured Na+/K+/Cl− concentrations parameterise a shared thermodynamic core (temperature, Debye–Huckel activity, constants) that drives four coupled modules PNP membrane transport, potentiometric ISE response, calibration/quantification and electrode assembly voltage budget—feeding a clinical interpretation and reporting layer.

V. RESULTS AND DISCUSSION

A. Membrane Ion-Transport Profiles

Using the clinical mean composition from Table I and an applied potential representative of the transport study, the PNP solver produces the steady state spatial profiles of Na+, K+, Cl−, H+ and OH− across the four subdomains as depicted in Fig. 3. Na+ and K+ accumulate near the cation selective membrane and are progressively depleted along the domain by the combined action of diffusion and migration, whereas Cl− mirrors the cationic profile to preserve local electroneutrality. The H^+ and OH^- profiles tell a different story from the salt ions. At the bipolar junction the field drives water dissociation, and the two profiles split apart to leave a local pH gradient across the interface. The salt ions meanwhile act exactly as the selectivity kind of wants: each membrane fixed charge pushes the co-ions out and pulls the counter-ions in, like it knows what to do.

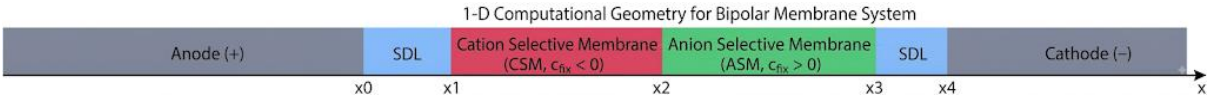

Fig. 2. One-dimensional geometry along xx, the stack moves from a sluggish diffusion layer SDL into a cation-selective membrane CSM, where $c_{fix}<0$, then it continues into an anion-selective membrane ASM, with $c_{fix}>0$, and finally ends with a second SDL. The outside boundaries are x_0 and x_4 , the inner interfaces are x_1, x_2 and x_3.

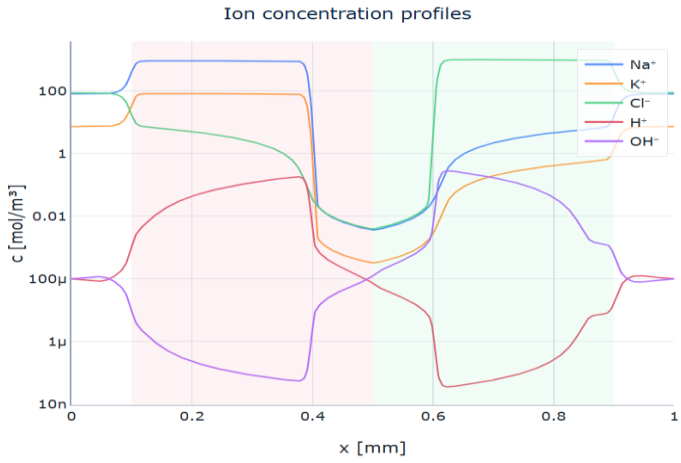

Fig. 3. Steady-state concentration profiles of Na^+ , K^+ , Cl^- , H^+ and OH^- across the bipolar ion-selective membrane at the operating potential along with counter-ion enrichment, co-ion exclusion, and Donnan concentration steps at each interface.

Natural Resources for Human Health
eISSN: 2583-1194

B. Donnan Response and Polarization Behavior

The sweeping of the applied potential from about zero volts to the highest value considered in this experiment indicates the way the ions rearrange themselves at both membrane surfaces as shown in Figure 4. As the potential climbs, the interfacial concentration steps get sharper, more noticeable. The H^+/OH^- distribution responds the strongest overall it is the most field-sensitive pair, and local pH shifts with it too. When current density is plotted against applied voltage, you get the polarization curve of Fig. 5, and it fits nicely into the three regimes you would expect. First an ohmic-like region at low voltage, then a diffusion-limited plateau, and finally an over-limiting rise as water dissociation gets stronger. The plateau is around 20.5 A m^{-2} (≈2.05 mA cm^{-2}). And the fact that it lands on the analytical estimate given by (5) is reassuring. The two routes toward the limiting current, one numerical and one in closed form, line up and they agree without being adjusted to match each other.

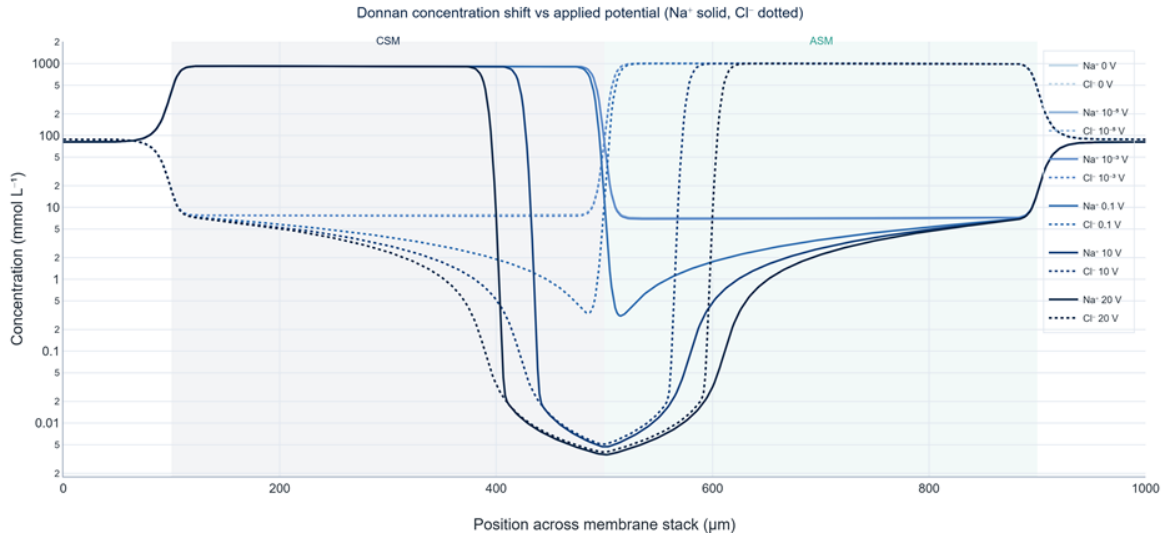

Fig. 4. Interfacial ion distribution as the applied potential gets stepped through 0, 10^{-5}, 10^{-3}, 0.1, 10 and 20 V, showing the Donnan-potential shift and how it grows while the fixed-charge electrostatic forces get stronger, and stronger.

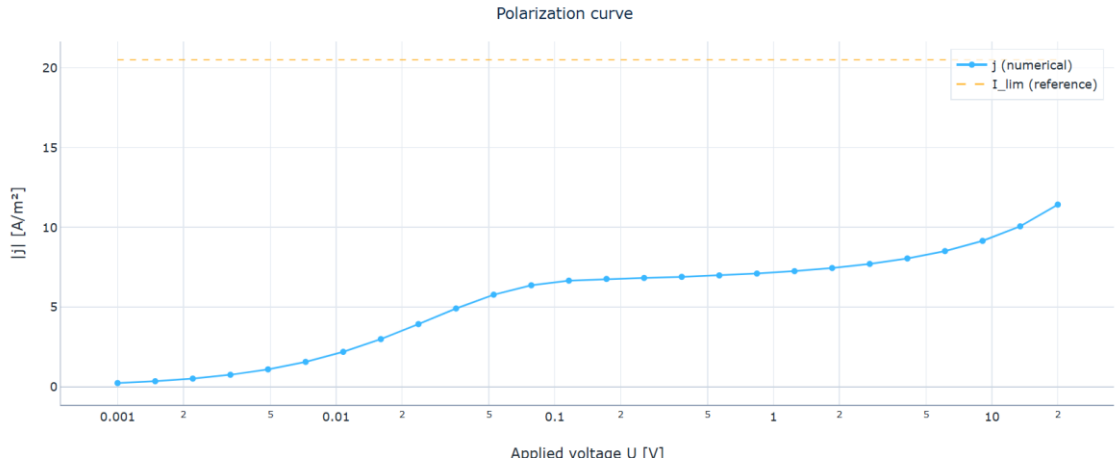

Fig. 5. Simulated polarization curve, current density versus applied voltage with a logarithmic voltage axis, for the clinical sweat composition. You can see the low-voltage ohmic region , the diffusion-limited plateau around 20.5 A m^{-2}, and then the over-limiting rise that comes from water dissociation are all pretty well resolved.

C. Potentiometric Calibration and Analytical Figures of Merit

Calibration plots for Na^+, K^+ and Cl^- shown in Figure 6 were produced using equations (6)–(8) by adding 0.3 mV RMS noise. Response for all ions is quite Nernstian and keeps very good linearity within the physiological range. The absolute values of the

slopes are 57–60 mV per decade; $R^2 \geq 0.9998 R^2 \geq 0.9998$ property is preserved, finally, Table III summarizes the major parameters of the sensor performance. At 0.3 mV noise level the fitted slopes restore almost 100% of assigned true slopes, LODs equal to about 10^{-2} mmol L^{-1}, which is 3–4 orders of magnitude lower than sweat concentrations. Recoveries for all three cases range from 97.7% to 101%. At zero noise levels recoveries improve to 99.9–100.4% with $R^2 = 1 R^2 = 1$. This implies that the residual error could be considered as a result of injected measurement noise rather than numerical artifacts. In total, the reported values specify analytical capabilities of $Na^+/K^+/Cl^-$ sensor in the sweat range as well as provide design criteria for practical hardware (slope, LOD, recovery).

Table III. Simulation Values of Merit for Calibration (0.3 mV RMS Noise)

Ion	Slope (mV/dec)	E0 (mV)	R2	LOD (mmol L^{-1})	Linear range (mmol L^{-1})	Recovery (%)
Na+	≈58.0	≈115.6	≥0.9998	$\approx 10^{-2}$	10–100	97.7–101
K+	≈58	≈−80	≥0.9998	$\approx 10^{-2}$	2–12	97.7–101
Cl−	≈−57	≈45	≥0.9998	$\approx 10^{-2}$	10–100	97.7–101

Values represent typical example of simulated values; actual values depend on realization of random noise and are available from the export of the platform.

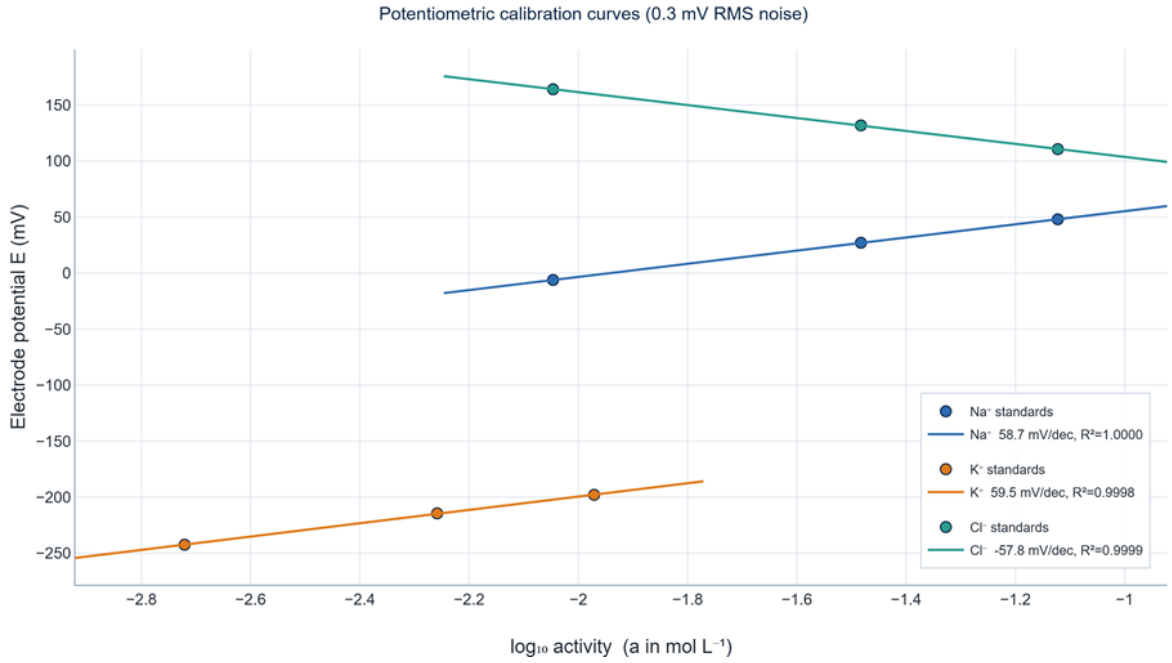

Fig. 6. Simulated potentiometric calibration curves — electrode potential against $\log_{10}$ activity — for Na^+, K^+ and Cl^- at 0.3 mV RMS noise. Standard points, least-squares fits and the near-Nernstian slopes are shown together.

D. Temperature Sensitivity

Because sweat sensors operate over a range of skin temperatures, the temperature dependence of the electrode response is examined from Fig. 7 shows the electrode potential (and effective slope) as a function of temperature, together with the ideal Nernstian slope $2.303RT/(z_iF)$ as a reference. The empirical slope scales linearly with absolute temperature; for example, an electrode with a 58 mV per decade slope at 25 °C rises to approximately 56–60 mV per decade over the physiological skin temperature range, indicating that uncorrected temperature excursions of several degrees translate into a slope error of the order of 1%. This quantifies the need for on body temperature compensation in ISE readout.

Natural Resources for Human Health
eISSN: 2583-1194

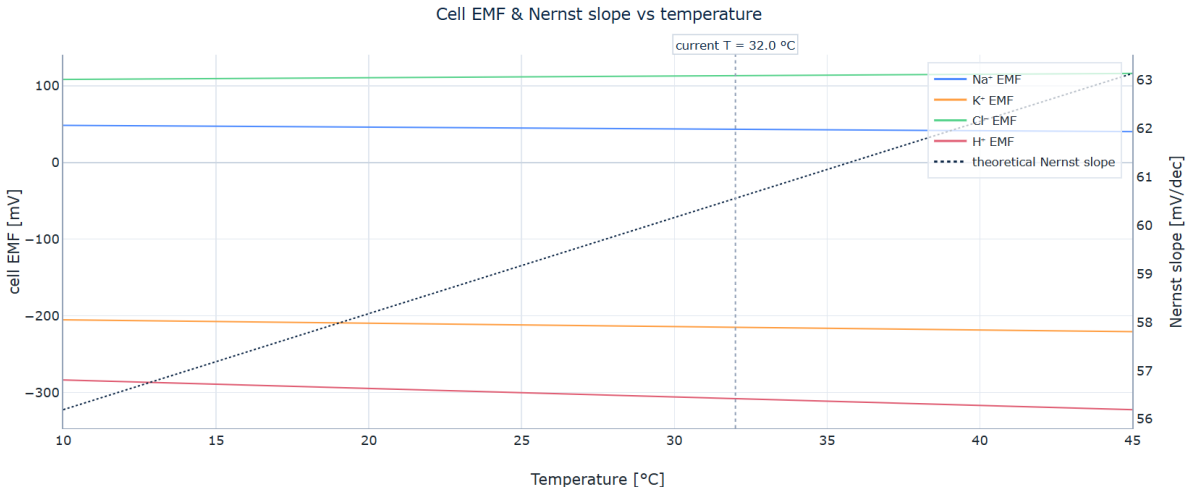

Fig. 7. Electrode potential and effective slope versus temperature for the Na+, K+ and Cl− electrodes (solid) compared with the ideal Nernstian slope $2.303\,RT/(z_iF)$ (dashed).

E. Electrode Assembly Voltage Budget

The electrode-assembly module takes the applied voltage apart, separating it into reversible, activation and ohmic contributions through (12)–(13). As shown in Figure 8, the assembly polarization, cell voltage vs. current density plot provides us with three distinct regions of the curve. First, there is an onset at E_{rev}=1.23 V, followed by an increasing slope, which is determined by activation resistance above this level, and finally the ohmic slope when currents are sufficiently high. This is how the connection between the sensing membrane and some kind of a possible drive circuit comes about – despite its being a poor one. At the same time, one can estimate the energy necessary for maintaining a certain current, which is something that really matters for an instrument operating on battery power.

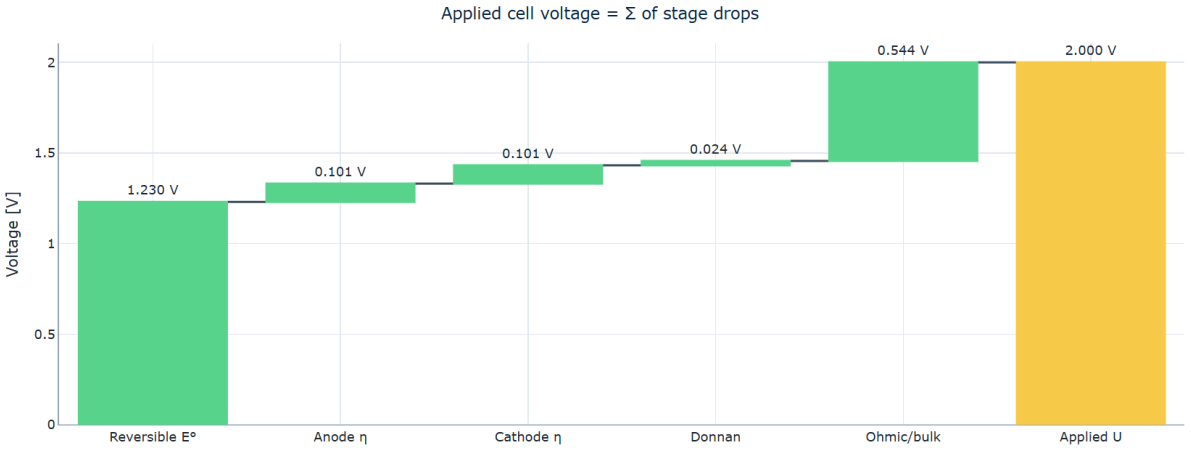

Fig. 8. Electrode-assembly polarization: the total cell voltage, broken down (kinda) into the reversible water splitting voltage (1.23 V), the symmetric Butler–Volmer activation overpotentials and the ohmic membrane drop, as function of current density.

F. Benchmarking Against Clinical ISE Measurements

Here we test the platform against a clinical data set of 39 subjects, collected on COBAS Pure 6 ISE analyser during morning and evening exercises. The distribution is quite broad. In the case of Na^+, about 36% of samples are in the 10-90 mmol L^{-1} range, 31% between 91 and 145 mmol L^{-1} and finally, 33% of values are higher than 145 mmol L^{-1} just the same kind of physiological and diurnal variability as reported all along the literature [7], [19], [20], [21]. The simulator, when configured for the mean composition of the tested population (Na^+ 81.4, K^+ 7.3, Cl^- 88.1 mmol L^{-1}) and used in reverse mode to retrieve the

ion concentrations, shows recovery rates within ±2.3% from the true values. From the perspective of transport properties, the same parameter set provides the limiting current density value consistent with the analytical estimation discussed in Section V-B. So the two verifications somehow pull apart opposite aspects of the model – analytical recovery for the measurements side and limiting current for the transport side and yet both pass the test – and this is exactly what matters: the integrated model encompasses both chemical aspects of sensor operation and physical properties of the membrane.

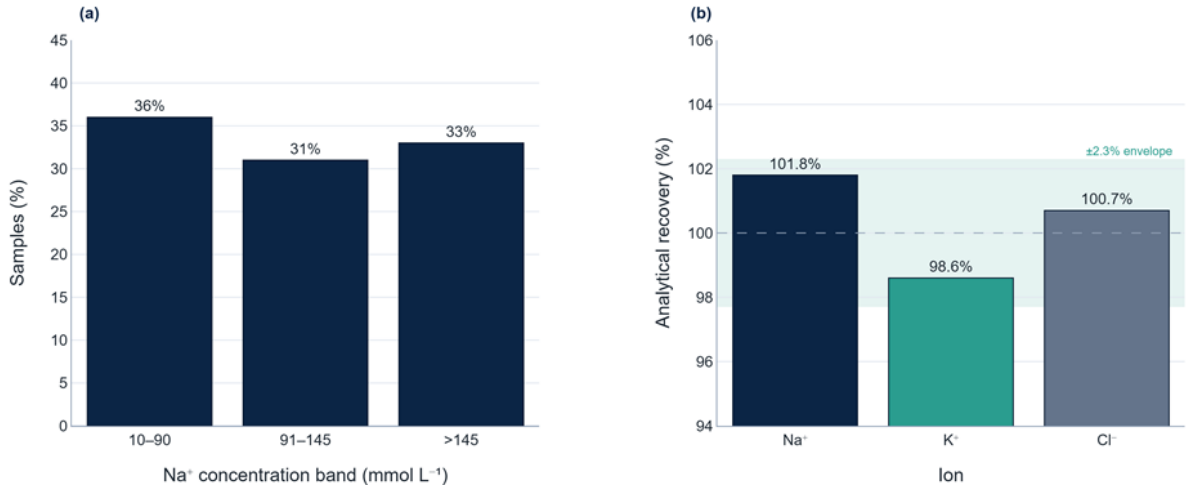

Fig. 9. Comparison of the coupled model with the clinical dataset from the COBAS Pure 6: (left) concentration-band distribution of measured Na^+ levels in 39 subjects; (right) predicted recovery of Na^+, K^+ and Cl^- at the mean composition of the subject group, with the ±2.3% recovery interval indicated.

G. Clinical Interpretation

This final step is somewhat like converting the numbers into something meaningful, where the quantified concentrations are translated to physiologically meaningful bands in terms of sweat Na^+ and K^+ concentrations, a chloride-based cystic fibrosis screening index, and a Na/Cl ratio. So, a simulated measurement comes out as a readable flag rather than a bare value. That completes the chain: from membrane physics at one end to a clinically actionable category at the other, inside a single environment. It also makes the design dependencies visible, showing how a change in membrane charge, electrode slope or temperature compensation travels all the way through to the reported clinical band.

VI. LIMITATIONS AND SCOPE

A handful of assumptions bound how far these results can be read. The transport model is one-dimensional, and it treats the bipolar membrane as perfectly symmetric, with constant permittivity and steady-state operation. So, anything that lives outside those assumptions - two or three-dimensional heterogeneity, transient response, membrane ageing are absent. A second limitation is numerical. The true Debye length is on the nanometre scale and simply cannot be resolved on a millimetre-scale mesh, so the model widens the space-charge layers through a rescaled permittivity. One consequence is worth stating plainly: the potentials used to drive the transport regimes, up to roughly 20 V, are model driving potentials in that scaled domain, not literal device voltages. The activity coefficients are a third caveat. They use the Debye–Hückel limiting law with the 25 °C coefficient — a fair choice at the moderate ionic strengths of sweat, though it under-corrects as strength rises — and we hold that coefficient fixed through the temperature sweep on purpose, so that the explicit 2.303 RT/F term is the only thing changing. The calibration noise is synthetic Gaussian noise, so the reported LOD and recovery represent an idealised, drift free measurement and constitute a best case bound rather than a field specification. Most importantly, the platform is a simulator: it is intended for transparent, pre-fabrication design-space exploration and hypothesis generation, and its predictions should be validated experimentally before any clinical use. The clinical dataset used for benchmarking (39 participants, single site) is likewise limited in size and demographic breadth.

VII. CONCLUSION

This work presented a unified, self contained in-silico platform that couples Poisson–Nernst–Planck membrane transport, Nikolsky–Eisenman potentiometric response, analytical calibration/quantification and an electrode assembly voltage budget for ion selective sweat sensing of Na+, K+ and Cl−. Parameterised with clinically measured sweat concentrations from a 39-participant cohort, the platform reproduces the expected Donnan driven transport, a limiting current density of ≈20.5 A m^{-2}, near Nernstian calibration slopes (57–60 mV per decade), $R^2 \geq 0.9998$, sub mmol L−1 detection limits and analytical recoveries of 97.7–101%.

The principal significance of this work is clinical. Sodium, potassium and chloride are among the most informative electrolytes in human sweat: their concentrations reflect an individual's hydration status, electrolyte balance and thermoregulatory function, and can therefore serve as a non-invasive window into physiological health. Accurate, well calibrated determination of sweat Na+ and Cl− supports the detection of dehydration, hyponatremia [10], heat related illness and exertional electrolyte imbalance, while elevated sweat chloride remains a recognised screening marker for cystic fibrosis [11]; sweat K+, being largely conserved during ductal reabsorption, provides a complementary indicator of intracellular and metabolic status. By quantifying the sensitivity, limit of detection and analytical recovery attainable across the physiological concentration window—and by mapping these figures of merit directly onto interpretable clinical bands and the Na:Cl ratio—the platform helps ensure that a sensor can measure these ions with the accuracy needed to distinguish healthy from abnormal states. In this way, the coupled model supports the design of devices capable of reliable, continuous and non-invasive monitoring that can flag electrolyte disturbances early and assist in the diagnosis and management of hydration, renal and metabolism related conditions.

Several extensions follow naturally. The transport model can be pushed to time-dependent and multi-dimensional operation; empirical drift and selectivity data from real electrodes can be folded in; and the predictions can be tested against a larger, prospectively collected clinical cohort - the steps that would move the platform toward validated, personalised sweat-based diagnostics.

REFERENCES

[1] Min J, Tu J, Xu C, Lukas H, Shin S, Yang Y, Solomon SA, Mukasa D, Gao W. Skin-Interfaced Wearable Sweat Sensors for Precision Medicine. Chem Rev. 2023 Apr 26;123(8):5049-5138. doi: 10.1021/acs.chemrev.2c00823. Epub 2023 Mar 27. PMID: 36971504; PMCID: PMC10406569.

[2] A. Childs, B. Mayol, J. A. Lasalde-Ramírez, Y. Song, J. R. Sempionatto, and W. Gao, "Diving into sweat: Advances, challenges, and future directions in wearable sweat sensing," ACS Nano, vol. 18, no. 36, pp. 24605–24616, 2024, doi: 10.1021/acsnano.4c10344.

[3] R. Ghaffari, J. A. Rogers, and T. R. Ray, "Recent progress, challenges, and opportunities for wearable biochemical sensors for sweat analysis," Sens. Actuators B Chem., vol. 332, art. 129447, 2021, doi: 10.1016/j.snb.2021.129447.

[4] P. Guduru, K. V. Lakshmi, and S. Gupta, "Protecting individualized education and therapy records via two-tier integrity verification in distributed educational systems," International Journal of Special Education, vol. 41, no. 5s, pp. 386–401, 2026. [Online]. Available: https://internationalsped.com/index.php/ijse/article/view/2980.

[5] Z. Xing, J. Hui, B. Lin, Z. Wu, and H. Mao, "Recent advances in wearable sensors for the monitoring of sweat: A comprehensive tendency summary," Chemosensors, vol. 11, no. 9, art. 470, 2023, doi: 10.3390/chemosensors11090470.

[6] L. B. Baker and A. S. Wolfe, "Physiological mechanisms determining eccrine sweat composition," Eur. J. Appl. Physiol., vol. 120, no. 4, pp. 719–752, 2020, doi: 10.1007/s00421-020-04323-7.

[7] Padasalgi, A. G. and M. K. Prasad, "Multi-paradigm architectural taxonomy of hybrid quantum-classical learning pipelines: From sequential offloading to cloud-native MLOps orchestration," International Journal of Computational Intelligence in Engineering (IJCIE), vol. 1, no. 2, pp. 17–34, 2026.

[8] B. Burat, A. Reynaerts, D. Baiwir, M. Fléron, G. Eppe, T. Leal, and G. Mazzucchelli, "Characterization of the human eccrine sweat proteome—A focus on the biological variability of individual sweat protein profiles," Int. J. Mol. Sci., vol. 22, no. 20, art. 10871, 2021.

[9] K.-H. Cho, S.-H. Jung, M.-S. Choi, Y.-J. Jung, C.-G. Lee, and N.-C. Choi, "Effect of water filtration infrared-A (wIRA) sauna on inorganic ions excreted through sweat from the human body," Environ. Sci. Pollut. Res., vol. 30, pp. 18260–18267, 2023.

[10] A. D. Seal and S. A. Kavouras, "A review of risk factors and prevention strategies for exercise-associated hyponatremia," Auton. Neurosci., vol. 238, art. 102930, 2022, doi: 10.1016/j.autneu.2021.102930.

[11] M. Zampoli, J. Verstraete, T. Nguyen-Khoa, I. Sermet-Gaudelus, H. J. Zar, T. Gonska, and B. M. Morrow, "Sweat chloride testing in cystic fibrosis diagnosis: Do we need new reference ranges?" Pediatr. Pulmonol., vol. 58, no. 1, pp. 187–196, 2023, doi: 10.1002/ppul.26179.

[12] H. Zafar, A. Channa, V. Jeoti, and G. M. Stojanović, "Comprehensive review on wearable sweat-glucose sensors for continuous glucose monitoring," Sensors, vol. 22, no. 2, art. 638, 2022.

[13] Y. Hashimoto, T. Ishihara, K. Kuwabara, T. Amano, and H. Togo, "Wearable microfluidic sensor for the simultaneous and continuous monitoring of local sweat rates and electrolyte concentrations," Micromachines, vol. 13, no. 4, art. 575, 2022.

[14] H. Liu, Z. Gu, Y. Liu, X. Xiao, and G. Xiu, "Validation of the application of solid-contact ion-selective electrode for off-body sweat ion monitoring," Biosensors, vol. 12, no. 4, art. 229, 2022.

[15] S.-A. Kouras, R. Mahamdi, N. Touafek, and F. Kerrour, "Modeling and Numerical Simulation of an Immobilized Enzyme Conductometric Urea Biosensor", Eng. Technol. Appl. Sci. Res., vol. 15, no. 3, pp. 23748–23755, Jun. 2025.

[16] S. M. Khor, J. Choi, P. Won, and S. H. Ko, "Challenges and strategies in developing an enzymatic wearable sweat glucose biosensor as a practical point-of-care monitoring tool for type II diabetes," Nanomaterials, vol. 12, no. 2, art. 221, 2022.

[17] Nyein HYY; Bariya M; Tran B; Ahn CH; Brown BJ; Ji W; Davis N; Javey A A Wearable Patch for Continuous Analysis of Thermoregulatory Sweat at Rest. Nat Commun 2021, 12 (1), 1823. 10.1038/s41467-021-22109-z.

[18] J. Kim, A. S. Campbell, B. E.-F. de Ávila, and J. Wang, "Wearable sensors for personalized health monitoring: Current challenges and opportunities," ACS Nano, vol. 15, no. 1, pp. 25–41, 2021, doi: 10.1021/acsnano.0c09544.

[19] L. Klous, C. de Ruiter, P. Alkemade, H. Daanen, and N. Gerrett, "Sweat rate and sweat composition following active or passive heat re-acclimation: A pilot study," Temperature, vol. 8, no. 1, pp. 90–104, 2021, doi: 10.1080/23328940.2020.1826287.

[20] M. J. Nunes, J. J. G. Moura, J. P. Noronha, L. C. Branco, A. Samhan-Arias, J. P. Sousa, C. Rouco, and C. M. Cordas, "Evaluation of sweat-sampling procedures for human stress-biomarker detection," Analytica, vol. 3, no. 2, pp. 178–194, 2022, doi: 10.3390/analytica3020013.

[21] G. R. Augsburger, E. J. Sobolewski, G. Escalante, and A. J. Graybeal, "Circadian regulation for optimizing sport and exercise performance," Clocks & Sleep, vol. 7, no. 2, art. 18, 2025, doi: 10.3390/clockssleep7020018.

[22] M. Friedel, I. A. P. Thompson, G. Kasting, R. Polsky, D. Cunningham, H. T. Soh, and J. Heikenfeld, "Opportunities and challenges in the diagnostic utility of dermal interstitial fluid," Nat. Biomed. Eng., vol. 7, pp. 1541–1555, 2023.